

## Supramolecular tuning of supported metal phthalocyanine catalysts for hydrogen peroxide electrosynthesis

**Authors:** Byoung-Hoon Lee<sup>1,7</sup>, Heejong Shin<sup>2,3,7</sup>, Armin Sedighian Rasouli<sup>1,7</sup>, Hitarth Choubisa<sup>1,7</sup>, Pengfei Ou<sup>1</sup>, Roham Dorakhan<sup>1</sup>, Ivan Grigioni<sup>1</sup>, Geonhui Lee<sup>1</sup>, Erfan Shirzadi<sup>1</sup>, Rui Kai Miao<sup>4</sup>, Joshua Wicks<sup>1</sup>, Sungjin Park<sup>1</sup>, Hyeon Seok Lee<sup>2,3</sup>, Jinqiang Zhang<sup>1</sup>, Yuanjun Chen<sup>1</sup>, Zhu Chen<sup>1</sup>, David Sinton<sup>4</sup>, Taeghwan Hyeon<sup>2,3\*</sup>, Yung-Eun Sung<sup>2,3\*</sup> and Edward H. Sargent<sup>1,5,6\*</sup>

### Affiliations:

<sup>1</sup>Department of Electrical and Computer Engineering, University of Toronto, Toronto, Ontario, Canada.

<sup>2</sup>Center for Nanoparticle Research, Institute for Basic Science (IBS), Seoul 08826, Republic of Korea.

<sup>3</sup>School of Chemical and Biological Engineering, and Institute of Chemical Processes, Seoul National University, Seoul 08826, Republic of Korea.

<sup>4</sup>Department of Mechanical and Industrial Engineering, University of Toronto, Toronto, Ontario, Canada.

<sup>5</sup>Department of Chemistry, Northwestern University, Evanston, Illinois 60208, United States

<sup>6</sup>Department of Electrical and Computer Engineering, Northwestern University, Evanston, Illinois 60208, United States

<sup>7</sup>These authors contributed equally: Byoung-Hoon Lee, Heejong Shin, Armin Sedighian Rasouli, Hitarth Choubisa

\*Corresponding authors. Email: [ted.sargent@utoronto.ca](mailto:ted.sargent@utoronto.ca) (E.H.S); [ysung@snu.ac.kr](mailto:ysung@snu.ac.kr) (Y.-E.S.); [thyeon@snu.ac.kr](mailto:thyeon@snu.ac.kr) (T.H.)

## Abstract

Two-electron oxygen reduction offers a route to  $\text{H}_2\text{O}_2$  that is potentially cost-effective and less energy-intensive than the industrial anthraquinone process. However, the catalytic performance of the highest-performing prior heterogeneous electrocatalysts to  $\text{H}_2\text{O}_2$  has lain well below the  $>300 \text{ mA cm}^{-2}$  needed for capital efficiency. Herein, guided by computation, we present a supramolecular approach that utilizes oxygen functional groups in a carbon nanotube (CNT) substrate that – when coupled with a cobalt phthalocyanine (CoPc) catalyst – improve CoPc adsorption, preventing agglomeration; and that further generate an electron-deficient Co centre whose interaction with the key  $\text{H}_2\text{O}_2$  intermediate is tuned towards optimality. The catalysts exhibit an overpotential of 280 mV at  $300 \text{ mA cm}^{-2}$  with TOF over  $50 \text{ s}^{-1}$  in a neutral medium, an order of magnitude higher activity compared to the highest-performing prior  $\text{H}_2\text{O}_2$  electrocatalysts. This performance is sustained for over 100 h of operation.

## Introduction

H<sub>2</sub>O<sub>2</sub> is used in the semiconductor, chemical and medical industries, leading to ~5 million tons of present-day annual demand<sup>1-6</sup>. Industrial H<sub>2</sub>O<sub>2</sub> is synthesized using the anthraquinone process, a process that requires Pd and consists of hydrogenation, oxidation, extraction and solvent regeneration that make the overall process capital- and energy-intensive: H<sub>2</sub>O<sub>2</sub> produced in this way consumes ~ 67 GJ ton<sup>-1</sup>H<sub>2</sub>O<sub>2</sub> and costs ~ \$ 1,200 ton<sup>-1</sup>H<sub>2</sub>O<sub>2</sub><sup>1,2,6</sup>.

Electrochemical oxygen reduction to H<sub>2</sub>O<sub>2</sub> offers an alternative route to produce H<sub>2</sub>O<sub>2</sub> from O<sub>2</sub> and H<sub>2</sub>O, and with the prospect of lower energy intensity. Technoeconomic analysis (Supplementary note 1 and 2) shows that achieving an energy efficiency (EE) of at least 20% at a current density above 300 mA cm<sup>-2</sup> will be necessary to offer a route to economical renewably-powered H<sub>2</sub>O<sub>2</sub> electrosynthesis. Electrosynthesized H<sub>2</sub>O<sub>2</sub> should be salt-free considering that >95% of H<sub>2</sub>O<sub>2</sub> is used as pure aqueous solution<sup>1,8</sup>. Electrosynthesis has been shown under these desired neutral conditions in solid-state-electrolyte (SSE) cells<sup>8</sup>; however, neutral H<sub>2</sub>O<sub>2</sub> electrosynthesis has yet to be combined with productivity above >300 mA cm<sup>-2</sup> simultaneous with high energy efficiency. Developing efficient neutral catalysts that operate at practical rates is a desired, and to date unmet, need in the electrosynthesis of H<sub>2</sub>O<sub>2</sub>.

Both molecular and heterogeneous catalyst have been investigated in electrocatalysis<sup>8-11</sup>. Modulating the local structure around molecular electrocatalysts enables them to achieve high turnover frequencies (TOF)<sup>9-17</sup>; but this has so far been limited to low current densities (<5 mA cm<sup>-2</sup>)<sup>12-16</sup> because – above these levels – the molecular catalysts agglomerate into non-conducting arrangements<sup>17</sup>. Heterogeneous electrocatalysts have been developed for high current density regimes (>100 mA cm<sup>-2</sup>) by tailoring the energetics of reaction intermediates on the catalyst

surface using strain<sup>18-21</sup>, forming alloys<sup>22-25</sup>, incorporating heteroatom functional groups<sup>26,27</sup> and tuning local coordination structure of atomic active sites<sup>4,28,29</sup>. However, H<sub>2</sub>O<sub>2</sub> electrosynthesis still suffers from a higher than desired overpotential (> 500 mV) and, as a consequence, limited energy efficiency (EE) (~10%) when carried out at current densities higher than 50 mA cm<sup>-2</sup><sup>6,7,30-32</sup>. Here, we report a supramolecular strategy that results in an electronically-tuned molecular catalyst that exhibits high turnover frequency in high current density regimes (>100 mA cm<sup>-2</sup>) in neutral conditions. We find that the presence of oxygen functional groups on the CNT surface generates electron-deficient CoPc, and that this optimally modulates the interactions of CoPc with key H<sub>2</sub>O<sub>2</sub> intermediates. We observe maximum TOF over 55 s<sup>-1</sup> and achieve 300 mA cm<sup>-2</sup> with overpotential of 280 mV, leading to an energy-efficiency of 22 percent at 300 mA cm<sup>-2</sup>, sustained for 100 h of operation. Energy analysis reveals a total energy cost of 38 GJ ton<sup>-1</sup><sub>H<sub>2</sub>O<sub>2</sub></sub>, a 40% reduction relative to the 67 GJ ton<sup>-1</sup><sub>H<sub>2</sub>O<sub>2</sub></sub> used in the industrial anthraquinone process<sup>1</sup>.

## Results

### *Supramolecular tuning of molecular electrocatalyst*

Enabling molecular H<sub>2</sub>O<sub>2</sub> electrocatalysts to operate stably at industrially relevant rates (>300 mA cm<sup>-2</sup>) is critical to energy efficient combined with high H<sub>2</sub>O<sub>2</sub> productivity. Recent works in CO<sub>2</sub> electroreduction pursued atomic dispersion of molecular catalysts on carbon supports, avoiding thereby aggregation of the molecular catalysts<sup>33-36</sup>. Stabilization of metal phthalocyanine was driven by  $\pi$ - $\pi$  interaction, enabling CO<sub>2</sub> electroreduction current densities exceeding 200 mA cm<sup>-2</sup><sup>34,35</sup>; however, direct ligand tuning of molecular catalysts was required to tune catalytic performance<sup>35</sup>. We posited that tuning the  $\pi$ - $\pi$  interaction between an atomically-dispersed molecular electrocatalyst and the carbon surface would add a degree of freedom enabling us to

control activity and stability. Considering that dipole-induced dipole forces are stronger than London forces, we thought introducing oxygen functional groups to generate dipole moments on a carbon surface would strengthen  $\pi$ - $\pi$  interaction between metal phthalocyanine and carbon surface, thereby tuning the electron density of the catalyst's metal centre, and consequently tailor its interaction with key reaction intermediates. We pursued therefore a supramolecular approach to strengthen adsorption of the molecular catalyst to an oxidized carbon support and prevent agglomeration, a strategy wherein we would lever the oxygen binding affinity of the molecular catalyst's metal centre.

We began with investigating the effect of O functional groups on the adsorption of CoPc on CNT surfaces. Compared to CoPc on CNTs without O functional groups, the presence of the O functional group on the CNT surface generates stronger CoPc adsorption through dipole-induced dipole interactions as seen in more negative stabilization energies (Fig. 1A). To explore the influence of stronger  $\pi$ - $\pi$  interaction on the Co metal centre, we carried out density of states calculations on CoPc adsorbed on pristine CNT and epoxy group functionalized CNT surface (Fig. 1B and Supplementary fig. 1-5). The presence of the epoxy group on the CNT results in electron delocalization on the Co centre, downshifting the  $d$  band centre of Co (Fig. 1C). Accordingly, strong interactions of the CoPc carbon ring and the epoxy functionalized CNT surface give rise to a more electron-deficient Co centre, seen in a decrease in the Bader charge and electron density distribution (Fig. 1D, 1E and Supplementary fig. 10). We also observe that different oxygen functional groups (COOH, OH, C-O-C and C=O) on the CNT surface show similar enhancements in  $\pi$ - $\pi$  interactions and modifications to the electronic structure of the Co centre. Bader charge analysis shows that in each case the Co centre becomes more electron-deficient: C=O ( $-0.01e^-$ ), OH ( $-0.04e^-$ ), and C-O-C/COOH ( $-0.05e^-$ ) and the change in the Co charge is linearly correlated

with stabilization energy and  $\Delta G_{\text{OOH}^*}$ . The adsorption strength of the key  $\text{H}_2\text{O}_2$  intermediate ( $\text{OOH}^*$ ) is known to depend on the  $d$  band level of metal centre<sup>33,37,38</sup>. Specifically, a downshift in the Co  $d$  band centre relative to the Fermi level results in a downshift of the antibonding states, leading to a higher occupation, and thus weakening of the  $\text{OOH}^*$  adsorption energy. The weaker  $\text{OOH}^*$  adsorption on electron-deficient Co center is also reflected in the peak width of the  $s$  and/or  $p$  states of  $\text{OOH}^*$ . Sharp  $s$  and/or  $p$  states are observed in projected DOS results of  $\text{OOH}^*$ , indicating a weaker  $\text{OOH}^*$  adsorption (that is enhanced  $\Delta G_{\text{OOH}^*}$ ), on electron deficient Co center (Fig. 1F)<sup>39</sup>. From this we conclude that O functional groups on the CNT surface provide CoPc stabilization through a dipole-induced dipole interaction, and that this downshifts the  $d$  band centre and generates an electron-deficient Co centre, thus tuning the adsorption of the relevant  $\text{H}_2\text{O}_2$  intermediate.

The ORR pathway is characterized by the tendency to dissociate the O-O bond ( $\Delta G_{\text{OOH}^*}$ ) (Figure 1D, Supplementary fig. 6-9). Fig. 1G show a volcano plot for oxygen reduction for the cases of both 2 electron and 4 electron pathways, this as a function of  $\Delta G_{\text{OOH}^*}$ . CoPc is closer to the optimum  $\Delta G_{\text{OOH}^*}$  (4.11 eV) and has a lower  $\text{H}_2\text{O}_2$  overpotential (120 mV) compared to FePc and NiPc (3.33 and 4.70 eV). FePc has an oxophilic Fe centre and prefers to break O-O bonds, resulting in  $4e^-$  ORR, whereas NiPc is  $\text{H}_2\text{O}_2$  selective, albeit with a higher overpotential. Interestingly, introducing O functional groups on the CNT surface enables optimization of the  $\Delta G_{\text{OOH}^*}$  of CoPc. For instance,  $\Delta G_{\text{OOH}^*}$  increases from 4.11 to 4.14 (for C=O) and 4.18 eV (for OH), closely approaching to the optimum for  $\text{H}_2\text{O}_2$  production. On the other hand, increase in  $\Delta G_{\text{OOH}^*}$  for CoPc has a detrimental effect for the 4 electron pathway, descending the right side of the volcano slope (blue line). These results indicate that tuning the  $\pi$ - $\pi$  interaction via introducing O functional groups on CNT surface can suppress the 4 electron ORR while promoting  $\text{H}_2\text{O}_2$

production by generating an electron-deficient Co centre. CoPc achieves the volcano optimum when COOH or C-O-C groups are attached on the CNT surface. The presence of COOH/C-O-C on the CNT surface optimizes the Bader charge of the Co centre ( $-0.05e^-$ ) and  $\Delta G_{\text{OOH}^*}$  (4.22 eV), suggesting a near-zero overpotential. We further investigated the molecular interface tuning strategy for the case of FePc and NiPc. Introducing a COOH group on the CNT surface increases  $\Delta G_{\text{OOH}^*}$  on FePc; however, FePc still favours the  $4e^-$  pathway. In contrast, NiPc is on the other side of the volcano and  $\Delta G_{\text{OOH}^*}$  becomes even larger when introducing the COOH group leading to a higher overpotential. To understand this supramolecular electronic tuning of the Co centre by O functional groups in the substrate, we calculated and visualized the electron density of CoPc adsorbed on an epoxy-(C-O-C)-group-functionalized CNT surface, which is near the top of the volcano plot. The epoxy group results in a non-uniform charge distribution on the CNT surface, inducing dipole attractions between the carbon rings of CoPc and the CNT surface. The induced dipoles lead to an even stronger  $\pi$ - $\pi$  interaction between CoPc and the CNT surface, evident as electron loss on the CNT surface and electron gain on the carbon rings of CoPc (Figure 1E, Supplementary fig. 10).

These computational results indicate that introducing oxygen functional groups on the CNT surface impacts catalytic activity. They motivate creation of an electron-deficient Co centre, and seeking to increase  $\Delta G_{\text{OOH}^*}$  of CoPc by introducing an electron-withdrawing O functional group on the CNT surface (Fig. 2A). We pursued acidic CNT oxidation to introduce O functional groups to the CNT surface<sup>5</sup>.

### *Catalyst preparation and characterization*

We performed X-ray photoelectron spectroscopy (XPS) to investigate the change in concentration and type of oxygen functional groups during acid treatment of CNTs. O 1s XPS spectra show that CNTs initially have a 1 at% of O species, and this increases with acid treatment time, peaking after 48 h (Fig. 2D and Supplementary fig. 11). CNTs after 48 h (hereafter, CNT(O)) contain 8 at% O, which includes both C-O (for C-OH and C-O-C) and C=O (for COOH and C=O) (Supplementary fig. 11). Fourier-transform infrared spectroscopy (FTIR) shows that the majority of oxygen in pristine CNT exists as surface adsorbed H<sub>2</sub>O (Supplementary fig. 12). Transmission electron microscopy (TEM) and high-angle annular dark-field scanning transmission electron microscopy (HAADF-STEM) show no structural deformation during the acid treatment (Fig. 2B and Supplementary fig. 13). We deposited CoPc onto CNT and CNT(O) materials (Methods). CoPc-CNT(O), NiPc-CNT(O) and FePc-CNT(O) electrocatalysts were prepared using the same method (Supplementary fig. 14).

We studied CoPc-CNT(O) catalyst materials using HAADF-STEM and found that CoPc molecules are evenly dispersed on the CNT(O) surface (Fig. 2C). The electronic structure of the Co metal centre on both CoPc-CNT and CoPc-CNT(O) was examined using X-ray absorption near-edge structure (XANES) (Fig. 2E). The white-line in the Co K-edge spectrum of CoPc-CNT(O) exhibits an upshift to a higher binding energy, and higher absorption-edge energy compared to CoPc-CNT, indicating the electron-deficient nature of the Co centre of CoPc-CNT(O), which we assign to the presence of abundant oxygen functional groups on CNT(O). The Co spectrum in extended X-ray absorption fine-structure (EXAFS) analysis reveals no metallic cobalt or cobalt oxide-based nanoparticles on CoPc-CNT(O) and CoPc-CNT, indicating that CoPc maintains its molecular structure on the CNT surface (Fig. 2F). We conclude that introducing O functional groups on CNT surface lowers the charge density of Co centre in adsorbed CoPc



molecules, and it does so without directly modifying their molecular structure. Since our calculation indicates that electron-deficient CoPc should favour H<sub>2</sub>O<sub>2</sub> production, we prepared molecular electrocatalysts to investigate the electrochemical behaviour of CoPc-CNT(O) materials.

### *ORR performance measurement*

We examined catalytic activity using a rotating ring-disk electrode (RRDE) at 1,600 rpm in an O<sub>2</sub> saturated 0.1 M K<sub>2</sub>SO<sub>4</sub> electrolyte (Fig. 3A-C and Supplementary fig. 15-21). A metal loading of 6 wt% is measured for all the CoPc-CNT, CoPc-CNT(O), FePc-CNT(O) and NiPc-CNT(O). Both CoPc-CNT and CoPc-CNT(O) show enhanced H<sub>2</sub>O<sub>2</sub> production compared to CNT(O). CoPc-CNT(O) shows superior 2e<sup>-</sup> ORR performance, a finding we ascribe to its electron-deficient Co centre, resulting in a higher selectivity and activity in 2e<sup>-</sup> ORR than for the other catalysts<sup>2-8</sup>. RRDE measurements were also performed on FePc-CNT(O) and NiPc-CNT(O) electrocatalysts. FePc-CNT(O) is selective toward 4e<sup>-</sup> ORR, and NiPc-CNT(O) shows lower H<sub>2</sub>O<sub>2</sub> activity than other catalysts, although it is selective to 2e<sup>-</sup> ORR. To examine the electronic state of Co centres in electrochemical systems, we carried out cyclic voltammetry (CV) in an argon-saturated 0.1M K<sub>2</sub>SO<sub>4</sub> electrolyte (Fig. 3D and Supplementary note 3). CoPc-CNT shows a reversible redox peak at -0.11 V assigned to the Co<sup>2+</sup>/Co<sup>+</sup> redox reaction. Notably, the Co<sup>2+</sup>/Co<sup>+</sup> redox couple of CoPc-CNT(O) shifts to +0.03 V, indicating that the cobalt centre in CoPc-CNT(O) has a lower tendency to be oxidized, i.e. the cobalt centre in CoPc-CNT(O) is more electron deficient than in CoPc-CNT. No change in CV spectra of CoPc-CNT(O) was observed after ORR measurements, indicating that the molecular structure was preserved after operation (Supplementary fig. 22, 24).

For H<sub>2</sub>O<sub>2</sub> electrosynthesis in acidic and neutral condition, it is critical to promote the electrocatalytic inner-sphere electron transfer mechanism by facilitating the direct adsorption of oxygen reactant on the active sites (Supplementary Note 3)<sup>40,41</sup>. To verify whether Co sites play a leading role in catalytic performance for H<sub>2</sub>O<sub>2</sub> production, we used the reversible ferri-/ferrocyanide ([Fe(CN)<sub>6</sub>]<sup>3-/4-</sup>) redox system and conducted poisoning experiments on Co centres using CN<sup>-</sup> (Fig. 3E, Supplementary fig. 23 and 25). The ferrocyanide system evaluates outer-sphere electron transfers in the ORR pathway and does not impact direct adsorption sites such as Co centres. The rate constants of CNT(O) and CoPc-CNT(O) have negligible differences, though ORR activities of the catalysts are drastically different. Even the rate constant of CoPc-CNT is significantly lower than that of CNT(O). Furthermore, the acidic ORR performance of CoPc-CNT(O) shows a prominent H<sub>2</sub>O<sub>2</sub> current in contrast with the negligible activity of the CNT(O) (Supplementary fig. 26). Consequently, the high ORR performance of CoPc-CNT(O) and CoPc-CNT compared to CNT(O) is dominated by the direct adsorption of molecular oxygen on the Co centre. To investigate if the concept can be generalized to other carbon materials, we changed the carbon material to commercial Vulcan carbon doped with O and B, finding a similar trend in its stabilization of CoPc (Supplementary Fig. 27).

#### *Practical scale H<sub>2</sub>O<sub>2</sub> electrosynthesis*

A three-compartment flow cell configuration was employed to evaluate the ORR-to-H<sub>2</sub>O<sub>2</sub> performance and stability of CoPc-CNT(O) electrocatalysts at high current densities (Fig. 4A) in neutral electrolyte (1.0M Na<sub>2</sub>SO<sub>4</sub>). Both the CoPc-CNT and CoPc-CNT(O) exhibited significantly higher current densities compared to that of CNT(O) (best prior catalyst in literature), with faradaic efficiencies (FE) above 90% toward H<sub>2</sub>O<sub>2</sub> (Supplementary table 1). We observed an improvement

in H<sub>2</sub>O<sub>2</sub> onset overpotentials in CoPc-CNT(O) (25 mV) and CoPc-CNT (110 mV) catalysts compared to CNT(O) (180 mV) catalysts. CoPc-CNT(O) exhibits 300 mA cm<sup>-2</sup> with H<sub>2</sub>O<sub>2</sub> FE above 90% and overpotential of 280 mV, which is 2.7 and 12 fold enhancement compared to current densities of CoPc-CNT and CNT(O) at the same applied overpotential (280 mV, 113 and 25 mA cm<sup>-2</sup>), respectively. CoPc-CNT(O) catalysts reached a peak current density 440 mA cm<sup>-2</sup> with 330 mV overpotential. In contrast, CNT(O) required a substantially higher overpotential (580 mV) to achieve 200 mA cm<sup>-2</sup>.

To characterize the effect of CoPc concentration on CNT(O) surface, we performed H<sub>2</sub>O<sub>2</sub> electrosynthesis in three-compartment flow cell for CoPc-CNT(O) with varied CoPc concentration (1, 3, 6wt% denotes nominal loading, Supplementary note 4 includes details). Assuming all Co centres as active sites, the turnover frequencies (TOF) of CoPc-CNT(O) was highest at 1wt% loading, reaching 56 s<sup>-1</sup> at 230 mV overpotential (Fig. 4E, Supplementary fig. 28 and Supplementary note 4). The TOF values are higher than the reported TOFs of H<sub>2</sub>O<sub>2</sub> production on state-of-the-art electrocatalysts (Supplementary table 2)<sup>2-8</sup>. Note that CoPc-CNT(O)-1 wt% exhibits substantially higher H<sub>2</sub>O<sub>2</sub> production compared to CoPc-CNT-6wt%, both in terms of TOF and current density (56 and 7 s<sup>-1</sup> for TOF, 89 and 45 for current density at 230 mV overpotential), although actual CoPc loading is measured to be less than 1/3 from ICP-MS measurement (0.9 and 3.3 wt%). CoPc-CNT(O)-6wt% exhibits highest current density, achieving 300 mA cm<sup>-2</sup> at 280 mV overpotential.

Intrigued by these results, we performed H<sub>2</sub>O<sub>2</sub> electrosynthesis in a flow-cell with a 2 mm gap in 1 M Na<sub>2</sub>SO<sub>4</sub> electrolyte (Fig. 4B, Supplementary fig. 29, See methods for details). At the anode, IrO<sub>2</sub> catalyst materials were used for oxygen evolution. A full-cell voltage (E<sub>cell</sub>) of 2.5 V

(non-iR-corrected) was required to obtain  $300 \text{ mA cm}^{-2}$ , whereas CoPc-CNT and CNT(O) exhibited 113 and  $25 \text{ mA cm}^{-2}$ .  $\text{H}_2\text{O}_2$  electrosynthesis performance on CoPc-CNT(O) with different oxygen concentrations shows that high oxygen concentration on the CNT surface is needed for high performance in the high current density regime (Supplementary fig. 30). The stability of CoPc-CNT(O) was examined under a constant current density of  $300 \text{ mA cm}^{-2}$  and exhibited <2% change in  $E_{\text{cell}}$  and  $\text{H}_2\text{O}_2$  FE over 100 h of operation (Fig. 4C and Supplementary table 3). Co L 2,3-edge XAS spectra, Co K-edge XANES and EXAFS spectra of CoPc-CNT(O) catalyst after 100 h operation at  $300 \text{ mA cm}^{-2}$ , showing Co L-edge and Co K-edge spectra indicative of CoPc and show that these remain after 100 h  $\text{H}_2\text{O}_2$  electrosynthesis (Supplementary fig. 32 and 33). CoPc-CNT(O) produced 4.6 wt%  $\text{H}_2\text{O}_2$  solution, higher than the concentration of an initial  $\text{H}_2\text{O}_2$  stream solution (1-3 wt%) produced using the anthraquinone process<sup>1,8</sup>. In contrast with the anthraquinone process, the  $\text{H}_2\text{O}_2$  solution does not contain organic waste and metal impurities (< 1 ppm), potentially reducing purification, solvent regeneration, and concentration costs. We then turned to an SSE cell with the goal of electrosynthesizing pure  $\text{H}_2\text{O}_2$ . We used a 1.2 mm gap (Fig. 4D, Supplementary fig. 34 and Methods). We observed full cell voltage of 3.1 V (iR uncorrected) with pure  $\text{H}_2\text{O}_2$  productivity of  $2.6 \text{ mmol cm}^{-2}\text{h}^{-1}$  (or  $26.1 \text{ mol g}^{-1}\text{h}^{-1}$ ) using CoPc-CNT(O) catalyst. This saves 800 mV compared to CNT(O) catalyst at same applied current density of  $200 \text{ mA cm}^{-2}$ .

Techno-economic analysis derived from two-compartment electrolyser results estimated a plant-gate levelized cost for  $\text{H}_2\text{O}_2$  production using CoPc-CNT(O) at half the market price (\$ 590 compared to \$ 1200  $\text{ton}^{-1}\text{H}_2\text{O}_2$  on 100 wt% basis, Fig. 4F, 4G, Supplementary fig. 35-37, please find details of parameters and calculation processes used in economic analyses in Supplementary Note

1 and 2)<sup>8,42</sup>. Electrochemical ORR-to-H<sub>2</sub>O<sub>2</sub> via CoPc-CNT(O) requires 38 GJ ton<sup>-1</sup><sub>H<sub>2</sub>O<sub>2</sub></sub> compared to 67 GJ ton<sup>-1</sup><sub>H<sub>2</sub>O<sub>2</sub></sub> for the anthraquinone process.

## **Discussion**

In summary, a supramolecular approach was introduced toward the goal of efficient and scalable H<sub>2</sub>O<sub>2</sub> electrosynthesis. The strategy employed a molecular electrocatalyst: we found that the presence of oxygen functional groups on the CNT surface strengthens the  $\pi$ - $\pi$  interaction between CoPc and the carbon surface, thereby tuning the electron density of the Co centre, thusly tailoring its interaction with key OOH\* intermediate in a manner that favours H<sub>2</sub>O<sub>2</sub> electrosynthesis. The CoPc-CNT(O) catalyst exhibits an overpotential of 280 mV at 300 mA cm<sup>-2</sup> with TOF over 50 s<sup>-1</sup> and >90% selectivity toward H<sub>2</sub>O<sub>2</sub> in a neutral medium, an order of magnitude higher activity compared to the highest-performing prior H<sub>2</sub>O<sub>2</sub> electrocatalysts. The work contributes toward the future decarbonisation of H<sub>2</sub>O<sub>2</sub> production.

## Methods

### Preparation of molecular electrocatalysts

Multi-walled CNT, CoPc, FePc, NiPc, *N,N*-dimethylformamide (DMF) and ethanol were obtained from Sigma Aldrich and used without further purification. Synthesis of molecular electrocatalysts followed a two-step procedure. The first step is the oxidation of CNT, modified from previous reports. Briefly, 0.2 g of multi-walled CNT was added to 200 mL of HNO<sub>3</sub> aqueous solution (60 wt%)<sup>5</sup>. The reaction mixture was then heated to 80 °C for 48 h under vigorous magnetic stirring. Reaction products were centrifuged, washed with water and ethanol, and freeze-dried to give resultant CNT(O) powder. The second step is MPc (M=Co, Fe, Ni) adsorption on the CNT surface. Briefly, 30 mg of CNT(O) (for CoPc-CNT(O), FePc-CNT(O) and NiPc-CNT(O)) and CNT (for CoPc-CNT) were added in 20 mL DMF solution, which is referred to as solution 1. Meanwhile, a calculated amount of MPc (M=Co, Ni, Fe; 0.5, 1, 3, 6 wt%, nominal loading) was added in another DMF solution (20 mL), referred to as solution 2. Both solutions 1 and 2 were then sonicated for at least 30 min to disperse CNTs and MPcs in the DMF solution. Solution 2 was then added to solution 1 and the mixture was sonicated for at least 30 min. The resulting mixture solution was vigorously stirred for 24 h at room temperature. Final molecular electrocatalysts were obtained by freeze-drying the mixture solution after stirring. Synthesis of CoPc stabilized on functionalized VC was modified from previous report<sup>43</sup>. 1 g of Commercial carbon black (Vulcan XC-72, Fuel Cell Store) was first oxidized in a three-neck flask with nitric acid (12M, 400 mL). Afterwards, under well-dispersed stirring conditions, the temperature was fixed at 80°C for 24h with a reflux system. After oxidation, the slurry was taken out, centrifuged and washed with DI water and ethanol 2 times until the solution pH reaches neutral. The sample was dried at 70°C in a vacuum oven, and the resulting sample is denoted as VC(O). To synthesize the boron-doped carbon substrate, the as-obtained VC(O) was mixed with boric acid (1:20 weight ratio) powders and annealed in Ar conditions at 750°C for 2h with 10°C/min ramp speed. The resulting sample was washed with hot water 3 times to remove the remaining boron oxide and dried in vacuum oven at 70 °C overnight. Then the resulting powder was further annealed under mixed H<sub>2</sub>(5%)/Ar condition for 2h at 750°C, as called VC(B).

### Material characterization

TEM imaging was conducted on a JEOL EM-2010 microscope operated at 200 kV. Atomic-resolution imaging of CoPc-CNT(O), FePc-CNT(O) and NiPc-CNT(O) was performed using a spherical aberration-corrected JEM ARM-200F microscope (Cold FEG Type, JEOL). XPS measurements were conducted using the K-Alpha<sup>+</sup> XPS system (Thermo Fisher Scientific). X-ray absorption fine structure (XAFS) measurements were made at the 8C nano-probe XAFS beamline (BL8C) of Pohang Light Source (PLS-II) in the 3.0 GeV storage ring, with a ring current of 300mA. The X-ray beam was monochromated by a Si (111) double crystal where the beam intensity was reduced by 30% to eliminate higher-order harmonics. The X-ray beam was then delivered to a secondary source aperture where the beam size was adjusted to 0.3mm (v)×1mm (h). A high voltage (3,000 V) was applied to ionization chambers filled with N<sub>2</sub>/Ar

mixture gases to detect X-ray intensity. XAFS spectra were collected in both transmission and fluorescence modes.

### Electrochemical measurements

All electrochemical measurements were run using a conventional three-electrode cell configuration with an RRDE system (Pine Instruments Corporation) and a custom-made flow cell, modified from a previous report<sup>44</sup>. An autolab potentiostat (PGSTAT302N) was employed to record the electrochemical response. An RRDE (AFE8R4GCPT, Pine) with a glassy carbon (5 mm diameter) and a platinum ring electrode were used as working electrodes. Before measurement, the electrochemical cell was immersed in 0.5 M H<sub>2</sub>SO<sub>4</sub> for 10 minutes, and subsequently boiled in deionized water to remove trace amounts of impurities. The working electrode was also polished mechanically with an alumina suspension (Buehler) and rinsed. An Ag/AgCl electrode and graphite rod were used as the reference and counter electrodes, respectively. All potentials of the measured data were calibrated to the reversible hydrogen electrode. To prepare the ink, 5 mg of each catalyst was dispersed in 2 mL of isopropanol with ultrasonication for 10 min, followed by the addition of 50  $\mu$ L of Nafion ionomer (5 wt%, Sigma-Aldrich). To compare the intrinsic 2e<sup>-</sup> ORR performance, all catalysts were first evaluated in a standard RRDE setup. The well dispersed ink (4.03  $\mu$ L) was drop casted onto the disk electrode (50  $\mu$ g cm<sup>-2</sup>) spinning at a rate of 250 rpm to achieve uniform electrode coating. To avoid any possible risk of degradation of our molecular catalysts in an alcohol-based solution, the catalyst ink was used within 2 hours of dispersing the catalyst powder in the ink solution. All the electrocatalytic measurements were run at 298 K. Before the ORR measurement, we conducted pre-cycling steps from 0.05 to 1.0 V (vs. RHE) at a scan rate of 50 mV s<sup>-1</sup> in an Ar-saturated 0.1 M K<sub>2</sub>SO<sub>4</sub> electrolyte until stable voltammograms were achieved. The activated catalyst electrode was then transferred to an O<sub>2</sub>-saturated electrolyte and polarized from 1.0 V to 0.1 V at a scan rate of 5 mV s<sup>-1</sup> and a rotating speed of 1600 rpm while holding the potential of the platinum ring electrode at 1.2 V. The polarization curves were corrected by subtracting the current obtained in an Ar-saturated electrolyte from that measured in O<sub>2</sub>-saturated conditions. The obtained ring currents were also corrected using the collection efficiency to evaluate the overall performance. The H<sub>2</sub>O<sub>2</sub> selectivity can be calculated by the equation:

$$\text{Selectivity of H}_2\text{O}_2 (\%) = 200 \times (I_r/N) / (I_d + I_r/N)$$

where  $I_r$  and  $I_d$  denote the ring and disk current, respectively. The kinetic current ( $I_k$ ) was calculated by the following equation:

$$1/I_m = 1/I_l + 1/I_k$$

where  $I_m$  indicates the measured current and  $I_l$  is the limiting current. We obtained the limiting current from the Levich equations with the total electron transfer number ( $n$ ) from the RRDE setup, as it is difficult to determine the value of limiting current for the carbonaceous catalysts. The

$$I_l = 0.62 n F A D_o^{2/3} \omega^{1/2} \nu^{-1/6} C_o$$

Cyclic voltammetry (CV) was performed from -0.5 to 1.6 V (vs. RHE) at a scan rate of 200 mV s<sup>-1</sup> in Ar-saturated electrolyte to observe the redox behavior of cobalt sites. To investigate the role of cobalt sites, CV was also conducted from -0.2 V to 0.7 V (vs. Ag/AgCl) at a scan rate of 200 mV s<sup>-1</sup> in an Ar-saturated solution of 1.0 M KCl + 5 mM K<sub>3</sub>[Fe(CN)<sub>6</sub>] (≥99%, Sigma-Aldrich). For poisoning tests, O<sub>2</sub>-saturated 0.1 M K<sub>2</sub>SO<sub>4</sub> electrolyte dissolving 10 mM KCN (≥96%, Sigma-Aldrich) was used. *iR* correction was applied during the experiment with a solution resistance value obtained from electrochemical impedance spectroscopy at frequencies from 0.1 Hz to 100 kHz.

To quantify the amount of generated H<sub>2</sub>O<sub>2</sub> molecules and achieve high peroxide concentrations at industrially relevant production rates, we firstly performed electrosynthesis in a flow cell using custom-made cells. For the three-electrode system without the diffusion-limitation of reactant dioxygen molecules, around 0.2 mg cm<sup>-2</sup> of each catalyst was air-brushed onto a gas diffusion layer (GDL) as the cathode. The GDL was a JNT-30A carbon paper with a 20 wt% PTFE content. Around 1.0 mg cm<sup>-2</sup> of IrO<sub>2</sub> catalyst (Premetek) was loaded onto a JNT-30A GDL electrode as the anode for water oxidation. The two electrodes were placed on opposite sides of a 1.0 cm thick PEEK spacer with a hole for the reference electrode (Ag/AgCl, RE-1CP, ALS) to achieve a three-electrode cell configuration. The active catalyst area on the GDL was 1 x 1 cm<sup>2</sup>, which faced the electrolyte flow compartment. This three-electrode flow cell was operated with 1.0 M Na<sub>2</sub>SO<sub>4</sub> solution as both an anolyte and a catholyte, which were separated by a Nafion 115 membrane (1.5 x 1.5 cm<sup>2</sup>, DuPont) between PEEK spacer and anode bipolar plate.

For two-electrode flow cell measurements, the two electrodes with the same conditions were placed on opposite sides of one 0.2 cm thick PEEK spacer with 0.5 cm wide by 2.0 cm channels, separated by a Nafion 115 membrane (1.0 x 2.5 cm<sup>2</sup>) between spacer and anode electrode. At the cathode side, the flow rate of the electrolyte was roughly 2 mL min<sup>-1</sup> controlled using a peristaltic pump, and 40 sccm of O<sub>2</sub> gas was supplied through the flow field of the titanium bipolar plate. The anode was circulated with 1.0 M Na<sub>2</sub>SO<sub>4</sub> at the same flow rate. The flow cell was first stabilized by applying each potential for 10 minutes before collecting liquid products. The generated H<sub>2</sub>O<sub>2</sub> concentration was evaluated by titration with potassium permanganate (0.1 N KMnO<sub>4</sub>, Sigma-Aldrich). The Faradaic efficiency of H<sub>2</sub>O<sub>2</sub> in flow cell systems can be calculated by the equation:

$$\text{Faradaic efficiency of H}_2\text{O}_2 (\%) = 100 \times (I_r/N) / I_d$$

To obtain a highly concentrated H<sub>2</sub>O<sub>2</sub> solution, electrolyte was circulated on the cathode side. 100 μL of the concentrated electrolyte was used to assess the production rate for H<sub>2</sub>O<sub>2</sub> in our system.

For the solid-state electrolyte (SSE) cell for direct electrosynthesis of H<sub>2</sub>O<sub>2</sub> without electrolyte salts, an anion exchange membrane (Sustainion X37-50 Grade RT, Dioxide Materials, USA) and a Nafion 115 membrane were used. The middle SSE part (0.5 x 2.0 x 0.12 cm<sup>3</sup>) with sandwiched between these two membranes was filled with Dowex 50WX8 hydrogen form (200-400 mesh, Sigma-Aldrich) as solid ion conductors. DI water was supplied to this porous SSE using a syringe pump to bring out the generated H<sub>2</sub>O<sub>2</sub>. The active area of both electrodes is 1 cm<sup>2</sup>, same



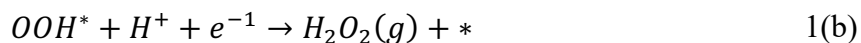
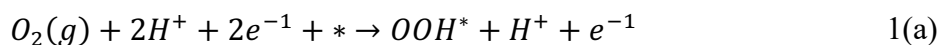
as above flow cell configurations (0.5 x 2 cm<sup>2</sup>). The cathode side was supplied with 40 sccm of humidified O<sub>2</sub> gas. The anode side was circulated with 0.5 M H<sub>2</sub>SO<sub>4</sub> at roughly 2 mL min<sup>-1</sup>. Before the collection of liquid product, the SSE chamber was stabilized for 30 minutes with a continuous DI water flow. The resistance of SSE cells was measured using the potentiostatic electrochemical impedance spectroscopy (EIS) method. In EIS results, the intersection of the curve with x-axis represents the testing resistance.

### Computational details on density functional theory (DFT) analysis

Slab models were built to simulate the catalysis conditions with MPc (M=Co, Ni, Fe) molecules adsorbed on the nanotube surface. 20Å of vacuum was added on top of the surface. All the DFT calculations were spin-polarized and performed using VASP<sup>45</sup> software package. AW pseudopotentials<sup>46</sup> and GGA<sup>47</sup> exchange-correlation (xc) functional with Many-body dispersion method were used for performing the calculations to accurately account for the  $\pi - \pi$  interactions and energy corrections<sup>48</sup>. Calculations were performed using preconditioned conjugated gradient (ALGO=A) and 1x1x1 Gamma k-point mesh with energy cut-off of 520 eV and Gaussian smearing of 0.05 eV. The validity of the Gamma-point calculation was verified both through performing a relaxation on a denser 1 × 3 × 3 grid and comparing the results. We observed that total energy from both set of calculations varied from each other by less than 0.05 eV for both the cases: pure C-N-O-H system as well as C-N-O-H-Co system. All the atoms were relaxed till the energy change was less than 10<sup>-4</sup> eV and the force on each atom was less than 0.03 eV/Å using the semi-local SCAN metaGGA xc-functional. Adsorption energies were calculated by using gas-phase H<sub>2</sub>O and H<sub>2</sub> as references. Free energies were obtained by applying zero-point energy and entropic corrections to the calculated DFT energies from previous studies<sup>49,50</sup>. In this study, we model effects of solvent using implicit solvation model as implemented in VaspSol<sup>51,52</sup>.

### ORR mechanism and calculation of reaction activation energies

Oxygen (O<sub>2</sub>) reduction to Hydrogen Peroxide (H<sub>2</sub>O<sub>2</sub>) follows a 2-electron reaction mechanism as,



Where \* denotes the catalyst and OOH\* denotes the intermediate adsorbed on the catalyst surface. The free energy change associated with both steps can therefore be expressed as,

$$\Delta G_{1a} = \Delta G_{ooh} - 4.92 \text{ (in eV)} \quad 1(c)$$

$$\Delta G_{1b} = 3.56 - \Delta G_{ooh} \text{ (in eV)} \quad 1(d)$$

Where  $\Delta G_{OOH}$  denotes adsorption energy of OOH intermediate species on the catalyst including the corrections induced by zero-point energy and entropic contributions.

The activation energy barrier associated with the reaction is then given by,

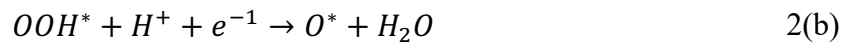
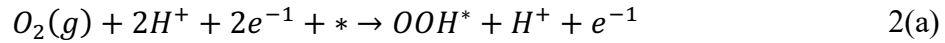
$$\Delta G = \max(\Delta G_{1a}, \Delta G_{1b})$$

In the presence of a non-zero electrode potential  $U$ , electron's energy is shifted by  $-eU$ <sup>44</sup>.

We can also correct the free energy of  $H^+$  ions by the concentration dependence of the entropy<sup>44</sup>:

$$\begin{aligned} G(\text{pH}) &= -kT \ln[H^+] = kT \ln 10 \times \text{pH} \\ &= 0.0259 \times 2.30258 \times \text{pH} \end{aligned} \quad 1(e)$$

For the 4-electron mechanism, the following set of reactions are used to model the process:



The corresponding free energy changes can then be expressed as,

$$\Delta G_{2a} = \Delta G_{ooh} - 4.92 \text{ (in eV)} \quad 2(e)$$

$$\Delta G_{2b} = \Delta G_o - \Delta G_{ooh} \text{ (in eV)} \quad 2(f)$$

$$\Delta G_{2c} = \Delta G_{oh} - \Delta G_o \text{ (in eV)} \quad 2(g)$$

$$\Delta G_{2d} = -\Delta G_{oh} \text{ (in eV)} \quad 2(h)$$

**Acknowledgements:** This work was supported by the Natural Gas Innovation Fund, the Natural Sciences and Engineering Research Council (NSERC) of Canada, the Natural Resources Canada Clean Growth Program, and the Ontario Research Fund—Research Excellence program. All DFT computations were performed on the Niagara supercomputer at the SciNet HPC Consortium. SciNet is funded by the Canada Foundation for Innovation, the Government of Ontario, the Ontario Research Fund Research Excellence Program, and the University of Toronto. This work was also supported by the Research Center Program of the IBS (IBS-R006-A2, Y.-E.S.; IBS-R006-D1, T.H) in Korea.

**Author contributions:**

E.H.S., Y.-E.S. and T.H. supervised the project. B.-H.L. conceived the idea. B.-H.L., H.S., A.S.R. and H.C. designed and performed the experiments. H.C. with the help of P.O. carried out DFT calculation. R.D., I.G., G.L., S.P., H.S.L., E.S., J.W., J.Z., C.C., and Y.C. contributed on material synthesis, characterization and electrochemical measurements. R.K.M. and D. S. assisted with electrochemical system design. B.-H.L., H.S., A.S.R., H.C., T.H., Y.-E.S. and E.H.S. wrote the manuscript. All authors commented on the manuscript.

**Competing interests:** The authors declare no competing interests.

**Data Availability:** The data supporting the findings of this study are provided with the paper and its Supplementary Information files. Further requests about data can be addressed to the corresponding authors.

**Additional Information:**

**Supplementary Information** is available in the online version of the paper.

**Correspondence and requests for materials** should be addressed to E.H.S., Y.-E.S. or T.H.

**Figure 1. Computational studies of electronically tuned H<sub>2</sub>O<sub>2</sub> molecular electrocatalysts.** (A) Relative stabilization energy of CoPc-CNT with COOH, OH, C-O-C or C=O group on the CNT surface. (B) Projected density of states of the CoPc molecule (pink), Co *d* bands (blue) and (C) Co *d* band centre of CoPc-CNT and CoPc-CNT with C-O-C group. (D) Calculated OOH\* adsorption energies and Bader charge of the Co centre in CoPc-CNT with various functional groups in CNT surface. (E) Top and side view of a calculated electron density distribution of CoPc-CNT after introducing epoxy (C-O-C) group on the CNT surface. Yellow and cyan isosurfaces show the electron gain and loss, respectively. (Brown, C; Red, O; Blue, Co; Grey, N; White, H). (F) Projected density of states of OOH\* adsorbed on CoPc-CNT and CoPc-CNT(C-O-C). (G) Calculated catalytic activity volcano for the production of H<sub>2</sub>O<sub>2</sub> via two electron (solid red line) and four electron ORR (solid blue line). The equilibrium potential for the two-electron and four-electron ORR is shown as the dashed grey line. Metal centres are the active sites under investigation (Fe, Co, and Ni).

**Figure 2. The synthesis and structural characterization of CoPc-CNT(O).** (A) Schematic of the catalyst/substrate interface for CoPc molecules deposited on oxygen functionalized CNT. (B) Low resolution TEM image of CNT(O) and (C) High-resolution HAADF-STEM image of CoPc-CNT(O). Yellow dotted circles represent isolated CoPc molecules on CNT(O) surface. (D) Oxygen contents of CNT and CNT(O) determined by O 1s spectra. (E) Co K-edge XANES spectra and (F) Co K-edge k<sup>3</sup>-weighted FT-EXAFS spectra in R space for CoPc-CNT(O), CoPc-CNT and Co foil.

**Figure 3. Electrochemical characterization of CoPc-CNT(O).** (A) Comparison of ORR performance at 1600 rpm (solid lines) and their H<sub>2</sub>O<sub>2</sub> detection current densities (dotted lines) at the ring electrode, and (B) H<sub>2</sub>O<sub>2</sub> FE over the applied potential range 0.2 V to 0.6 V. (C) Comparison of kinetic current densities measured at 0.45 V vs. RHE. The error bars correspond to the standard deviation of at least three independent measurements. (D) Cyclic voltammetry analysis of CoPc-CNT(O) and CoPc-CNT in Ar saturated 0.1M K<sub>2</sub>SO<sub>4</sub> solution. Dotted lines represent Co<sup>2+</sup>/Co<sup>+</sup> redox reaction of CoPc centre. (E) Rate constants derived from ferrocene cyclic voltammetry analysis of CoPc-CNT(O), CoPc-CNT and CNT(O).

**Figure 4. H<sub>2</sub>O<sub>2</sub> production performance in flow cells.** (A) Linear sweep voltammetry and H<sub>2</sub>O<sub>2</sub> FE of CoPc-CNT(O), CoPc-CNT and CNT(O) in 3-electrode flow cell (see method for details). The grey dotted line represents the thermodynamic onset potential of H<sub>2</sub>O<sub>2</sub>. (B) H<sub>2</sub>O<sub>2</sub> electrosynthesis in a two-compartment flow cell with 2 mm cm gap. (C) Long-term H<sub>2</sub>O<sub>2</sub> electrosynthesis at 300 mA cm<sup>-2</sup> in a two-compartment full cell device. (D) Pure H<sub>2</sub>O<sub>2</sub> production using a solid-state-electrolyte cell with 1.2 mm gap. (E) TOF of catalysts derived from three-compartment flow cell results. The error bars correspond to the standard deviation of at least three independent measurements. (F) Techno-economic analysis of H<sub>2</sub>O<sub>2</sub> electrosynthesis with two different conditions and (G) energy analysis derived from two-compartment full cell results.

## References

1. Merchant research and Consulting Ltd., hydrogen peroxide (HP): 2015 world market outlook. (2015). (Merchant Research and Consulting Ltd.).
2. Siahrostami, S. et al. A review on challenges and successes in atomic-scale design of catalysts for electrochemical synthesis of hydrogen peroxide. *ACS Catal.* **10**, 7495-7511 (2020).
3. Perry, S. C. et al. Electrochemical synthesis of hydrogen peroxide from water and oxygen. *Nat. Rev. Chem.* **3**, 442-458 (2019).
4. Jung, E. et al. Atomic-level tuning of Co-N-C catalyst for high-performance electrochemical H<sub>2</sub>O<sub>2</sub> production. *Nat. Mater.* **19**, 436-442 (2020).
5. Jung, E., Shin, H., Hooch Antink, W., Sung, Y. E. & Hyeon, T. Recent advances in electrochemical oxygen reduction to H<sub>2</sub>O<sub>2</sub>: Catalyst and cell design. *ACS Energy Lett.* **5**, 1881-1892 (2020).
6. Zhang, X. L. et al. Strongly coupled cobalt diselenide monolayers for selective electrocatalytic oxygen reduction to H<sub>2</sub>O<sub>2</sub> under acidic conditions. *Angew. Chem. Int. Ed.* **60**, 2-11 (2021).
7. Seh, Z. W. et al. Combining theory and experiment in electrocatalysis: Insights into materials design. *Science* **355**, eaad4998 (2017).
8. Xia, C., Xia, Y., Zhu, P., Fan, L. & Wang, H. Direct electrosynthesis of pure aqueous H<sub>2</sub>O<sub>2</sub> solutions up to 20% by weight using a solid electrolyte. *Science* **366**, 226-231 (2019).
9. Han, Z., Horak, K. T., Lee, H. B. & Agapie, T. Tetranuclear Manganese Models of the OEC displaying hydrogen bonding interactions: Application to electrocatalytic water oxidation to hydrogen peroxide. *J. Am. Chem. Soc.* **139**, 9108-9111 (2017).
10. Costentin, C., Drouet, S. Robert, M. & Saveant, J. M. A local proton source enhances CO<sub>2</sub> electroreduction to CO by a molecular Fe catalyst. *Science* **338**, 90-94 (2012).
11. Buss, J. A. & Agapie, T. Four-electron deoxygenative reductive coupling of carbon monoxide at a single metal site. *Nature* **529**, 72-75 (2016).
12. Liu, C. et al. Intrinsic activity of metal metal centers in metal-nitrogen-carbon single-atom catalysts for hydrogen peroxide synthesis. *J. Am. Chem. Soc.* **142**, 21861-21871 (2020).
13. Wang, Y. H., Pegis, M. L., Mayer, J. M. & Stahl, S. S. Molecular cobalt catalyst for O<sub>2</sub> reduction: Low-overpotential production of H<sub>2</sub>O<sub>2</sub> and comparison with Iron-based catalysts. *J. Am. Chem. Soc.* **139**, 16458-16461 (2017).
14. Honda, T., Kojima, T. & Fukuzumi, S. Proton-coupled electron-transfer reduction of dioxygen catalyzed by a saddle-distorted cobalt phthalocyanine. *J. Am. Chem. Soc.* **134**, 4196-4206 (2012).
15. Wu, Y., Jiang, Z., Lu, X., Liang, Y. & Wang, H. Domino electroreduction of CO<sub>2</sub> to methanol on a molecular catalyst. *Nature* **575**, 639-642 (2019).
16. Severy, L. et al. Immobilization of molecular catalysts on electrode surfaces using host-guest interactions. *Nat. Chem.* **13**, 523-529 (2021).
17. Zhu, M., Ye, R., Jin, K., Lazouski, N. & Manthiram, K. Elucidating the reactivity and mechanism of CO<sub>2</sub> electroreduction at highly dispersed cobalt phthalocyanine. *ACS Energy Lett.* **3**, 1381-1386 (2018).
18. Wang, H. et al. Direct and continuous strain control of catalysts with tunable battery electrode materials. *Science* **354**, 1031-1036 (2016).
19. He, T. et al. Mastering the surface strain of platinum catalysts for efficient electrocatalysis.

- Nature* **598**, 76-81 (2021).
20. Luo, M. et al. PdMo bimetallic for oxygen reduction catalysis. *Nature* **574**, 81-85 (2019).
  21. Bok, J. et al. Designing atomically dispersed Au on tensile-strained Pd for efficient CO<sub>2</sub> electroreduction to formate. *J. Am. Chem. Soc.* **143**, 5386-6395 (2021).
  22. Siahrostami, S. et al. Enabling direct H<sub>2</sub>O<sub>2</sub> production through rational electrocatalyst design. *Nat. Mater.* **12**, 1137-1143 (2013).
  23. Escudero-Escribano, M. et al. Tuning the activity of Pt alloy electrocatalysts by means of the lanthanide contraction. *Science* **352**, 73-76 (2016).
  24. Chen, C. et al. Highly crystalline multimetallic nanoframes with three-dimensional electrocatalytic surfaces. *Science* **343**, 1339-1343 (2014).
  25. Zhang, B. et al. Homogeneously dispersed multimetal oxygen-evolving catalysts. *Science* **352**, 333-337 (2016).
  26. Lu, Z. et al. High-efficiency oxygen reduction to hydrogen peroxide catalysed by oxidized carbon materials. *Nat. Catal.* **1**, 156-162 (2018).
  27. Guo, D. et al. Active sites of nitrogen-doped carbon materials for oxygen reduction reaction clarified using model catalysts. *Science* **351**, 361-365 (2016).
  28. Jiao, Y., Zheng, Y., Jaroniec, M. & Qiao, S. Z. Origin of the electrocatalytic oxygen reduction activity of graphene-based catalysts: A roadmap to achieve the best performance. *J. Am. Chem. Soc.* **136**, 4394-4403 (2014).
  29. Gu, J., Hsu, C. S., Bai, L., Chen, H. M. & Hu, X. Atomically dispersed Fe<sup>3+</sup> sites catalyze efficient CO<sub>2</sub> electroreduction to CO. *Science* **364**, 1091-1094 (2019).
  30. Chen, S. et al. Chemical identification of catalytically active sites on oxygen-doped carbon nanosheet to decipher the high activity for electro-synthesis hydrogen peroxide. *Angew. Chem. Int. Ed.* **60**, 16607-16614 (2021).
  31. Cao, P. et al. Durable and selective electrochemical H<sub>2</sub>O<sub>2</sub> synthesis under a large current enabled by the cathode with highly hydrophobic three-phase architecture. *ACS Catal.* **11**, 13797-13808 (2021).
  32. Zhao, Q. et al. Approaching a high-rate and sustainable production of hydrogen peroxide: oxygen reduction on Co-N-C single-atom electrocatalysts in simulated seawater. *Energy Environ. Sci.* **14**, 5444-5456 (2021).
  33. Pan, Y. et al. Design of single-atom Co-N<sub>5</sub> catalytic site: A robust electrocatalyst for CO<sub>2</sub> reduction with nearly 100% CO selectivity and remarkable stability. *J. Am. Chem. Soc.* **140**, 4218-4221 (2018).
  34. Ren, S. et al. Molecular electrocatalysts can mediate fast, selective CO<sub>2</sub> reduction in a flow cell. *Science* **365**, 367-369 (2019).
  35. Zhang, X. et al. Molecular engineering of dispersed nickel phthalocyanines on carbon nanotubes for selective CO<sub>2</sub> reduction. *Nat. Energy* **5**, 684-692 (2020).
  36. Schild, J. et al. Approaching industrially relevant current densities for hydrogen oxidation with a bioinspired molecular catalytic material. *J. Am. Chem. Soc.* **143**, 18150-18158 (2021).
  37. Jin, H. et al. Unprecedentedly high activity and selectivity for hydrogenation of nitroarenes with single atomic Co<sub>1</sub>-N<sub>3</sub>P<sub>1</sub> sites. *Nat. Commun.* **13**, 723 (2022).
  38. Mun, Y. et al. Versatile Strategy for Tuning ORR Activity of a Single Fe-N<sub>4</sub> Site by Controlling Electron-Withdrawing/Donating Properties of a Carbon Plane. *J. Am. Chem. Soc.* **141**, 6254-6262 (2019).
  39. Vijay, S. et al. Unified mechanistic understanding of CO<sub>2</sub> reduction to CO on transition

- metal and single atom catalysts. *Nat. Catal.* **4**, 1024-1031 (2021).
40. Ramaswamy, N. & Mukerjee, S. Influence of Inner- and Outer-Sphere Electron Transfer Mechanisms during Electrocatalysis of Oxygen Reduction in Alkaline Media *J. Phys. Chem. C* **115**, 18015-18026 (2011).
  41. Blizanac, B. B., Ross, P. N. & Markovic, N. M. Oxygen electroreduction on Ag(1 1 1): The pH effect *Electrochim. Acta* **52**, 2264-2271 (2007).
  42. Luna, P. D. et al. What would it take for renewably powered electrosynthesis to displace petrochemical processes? *Science* **364**, eaav3506 (2019).

### References for methods

43. Yu, X. et al. Boron-Doped Graphene for Electrocatalytic N<sub>2</sub> Reduction. *Joule* **2**, 1610-1622 (2018).
44. Wang, M. et al. CO<sub>2</sub> electrochemical catalytic reduction with a highly active cobalt phthalocyanine. *Nat. Commun.* **10**, 3602 (2019).
45. Kresse, G. & Furthmüller, J. Efficient iterative schemes for ab initio total-energy calculations using a plane-wave basis set. *Phys. Rev. B* **54**, 11169–11186 (1996).
46. Blöchl, P. E. Projector augmented-wave method. *Phys. Rev. B* **50**, 17953–17979 (1994)
47. Wang, L., Maxisch, T. & Ceder, G. Oxidation energies of transition metal oxides within the GGA+U framework. *Physical Review B* **73**, 195107 (2006)
48. Tkatchenko, A., DiStasio Jr, R. A., Car, R. & Scheffler, M. Accurate and Efficient Method for Many-Body van der Waals Interactions. *Phys. Rev. Lett.* **108**, 236402 (2012).
49. Man, I. C. et al. Universality in oxygen evolution electrocatalysis on oxide surfaces. *ChemCatChem* **3**, 1159–1165 (2011).
50. Nørskov, J. K. et al. Origin of the overpotential for oxygen reduction at a fuel-cell cathode. *J. Phys. Chem. B* **108**, 17886–17892 (2004).
51. Mathew, K. et al. Implicit solvation model for density-functional study of nanocrystal surfaces and reaction pathways. *J. Chem. Phys.* **140**, 084106 (2014).
52. Mathew, K. et al. Implicit self-consistent electrolyte model in plane-wave density-functional theory. *J. Chem. Phys.* **151**, 234101 (2019).